Topological insulators based on p-wave altermagnets, electrical control and detection of the altermagnetic domain wall

Motohiko Ezawa[1]

[1]*Department of Applied Physics, The University of Tokyo, 7-3-1 Hongo, Tokyo 113-8656, Japan*
(Dated: April 15, 2024)

We study a one-dimensional hybrid system made of a p-wave altermagnet and a metal possessing the orbital degree of freedom. The hybrid system is a topological insulator without the spin-orbit interaction. There emerge two edge states per one edge, because the system is mapped to a set of two copies of a topological insulator. Each copy resembles the long-range Su-Schrieffer-Heeger model but it is topologically different. Topological interface states emerge at a domain wall of the p-wave altermagnet, which are charged due to the Jackiw-Rebbi mechanism. Hence, the domain wall of the p-wave is controllable and detectable by purely electrical means.

Altermagnets are the third type of magnets from the viewpoint of symmetry[1–3]. They are expected to be key players of next generation memories because they have both merits of ferromagnets and antiferromagnets. The even-parity altermagnets including the d-wave, f-wave and i-wave altermagnets are main targets[4–16]. Recently, p-wave altermagnets were proposed[17]. The study of odd-parity altermagnets is just a beginning stage[18].

Magnetic domain walls are used for magnetic memories. For example, the magnetic race-track memory stores information by positions of domain walls[19, 20]. Readout and control of the position of the domain wall are essential. In ferromagnetic domain wall, it can be read out by observing magnetization. In addition, the position of the domain wall is shifted by applying a current due to the spin-transfer torque[21, 22]. On the other hand, it is difficult to read out and control the position of a domain wall of antiferromagnetic systems[23–29].

In the even-parity altermagnets, the magnetization is read out by anomalous Hall effects[4–7] because time-reversal symmetry is broken. However, this is not the case in the p-wave altermagnet because time-reversal symmetry is preserved. Then, it is a highly nontrivial problem to detect and control the magnetic domain wall made of the p-wave altermagnet. As far as we are aware of, there is no study on the topological property based on the p-wave altermagnet although there are some works[30–34] on the d-wave altermagnet.

In this paper, we study a hybrid system made of the p-wave altermagnet and one-dimensional metal possessing the orbital degree of freedom. We find the emergence of two-fold zero-energy topological edge states at each edge. It is understood by making a unitary transformation, where the system becomes a set of two copies of one-dimensional topological insulator model. This model resembles the long-range Su-Schrieffer-Heeger (SSH) model but its topological properties are different although both models belong to the same topological class BDI. Next, we show that the Jackiw-Rebbi interface states exist at the domain wall made of the p-wave altermagnet. Because they are charged, the domain-wall position is detected and controlled with the aid of electric field.

Model: We analyze the system where a one-dimensional metal with the orbital degree of freedom is attached to a p-
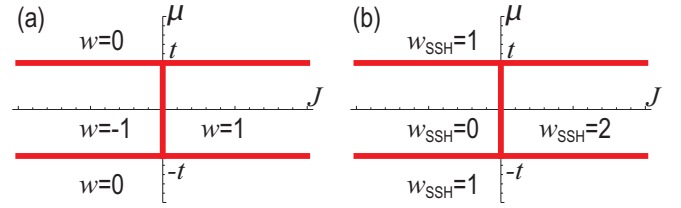

FIG. 1. Topological phase diagram in the J-μ plane for (a) the Hamiltonian H_0 and (b) the SSH Hamiltonian H_{SSH}.

wave altermagnet. The Hamiltonian is given by

$$H = \Gamma_{0z} \sum_x \frac{t}{2}\left(\hat{c}_x^\dagger \hat{c}_{x+1} + \hat{c}_{x+1}^\dagger \hat{c}_x\right) - \mu \hat{c}_x^\dagger \hat{c}_x$$
$$+ \Gamma_{zx}\frac{J}{2i}\sum_x \left(\hat{c}_x^\dagger \hat{c}_{x+1} - \hat{c}_{x+1}^\dagger \hat{c}_x\right), \qquad (1)$$

where $\Gamma_{\mu\nu} \equiv \sigma_\mu \otimes \tau_\nu$ is the gamma matrix with σ_μ the Pauli matrix for spins and τ_ν the Pauli matrix for orbitals; t is the hopping amplitude and μ is the chemical potential for the metallic wire, while J is the magnetization of the p-wave altermagnet. We note that there is no spin-orbit interaction in the Hamiltonian.

The Hamiltonian density reads in the momentum space as

$$H(k) = (t\cos k - \mu)\,\Gamma_{0z} + (J\sin k)\,\Gamma_{zx}, \qquad (2)$$

where k is the momentum along the x-direction, $0 \leq k < 2\pi$. The energy spectrum is given by

$$E(k) = \pm\sqrt{(t\cos k - \mu)^2 + (J\sin k)^2}, \qquad (3)$$

where the energy is two-fold degenerated. The gap closing conditions are given by $|\mu/t| = 1$ and $J = 0$ with $|\mu/t| < 1$, which are illustrated by red lines in the J-μ plane as in Fig.1(a).

Symmetry: The system has chiral symmetry $\{H, \Gamma\} = 0$ with the chiral operator $\Gamma \equiv [\Gamma_{0z}, \Gamma_{zx}]/2i$. It has also time-reversal symmetry $\Theta H(k)\,\Theta^{-1} = H(-k)$ with $\Theta = i\sigma_y$. In addition, there is particle-hole symmetry operator $\Xi H(k)\,\Xi^{-1} = -H(-k)$ with $\Xi = \tau_x$. Then, the system belongs to the class BDI, whose topology is characterized by the class $\mathbb{Z}$.
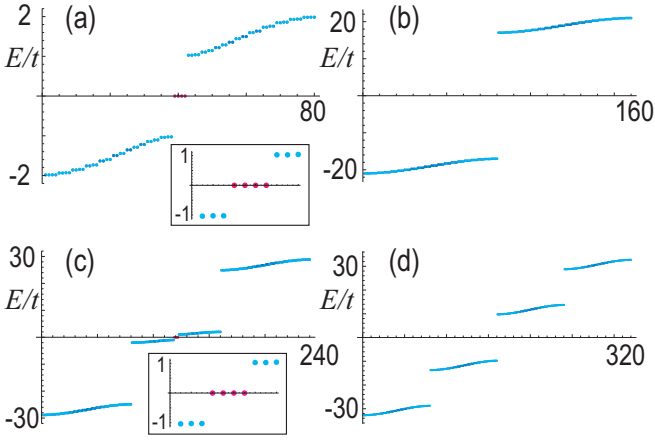
FIG. 2. Energy spectrum for a finite chain. The horizontal axis is the site index. (a) One-dimensional model described by Eq.(1), (b) nanoribbon described by Eq.(28) with $W = 2$, (b) nanoribbon with $W = 3$ and (b) nanoribbon with $W = 4$. Red color indicates the topological edge states, while cyan color indicates the bulk states. Insets in (a) and (c) show the enlarged energy spectrum in the vicinity of the zero energy. We have set $J = 0.5t$, $\mu = 0$ and $L = 20$.

Topological edge states: We study a chain with a finite length. The energy spectrum is shown in Fig.2(a). There emerge four zero-energy topological edge states as is clear in the inset of Fig.2(a), where two zero-energy edge states are present at each edge.

We show the energy spectrum as a function of J by setting $\mu = 0$ in Fig.3(a). The system is gapped for $J \neq 0$, where topological edge states emerge at the zero energy. There is a tiny gap around $J = 0$ in Fig.3(a), which is due to the finite-length effect owing to the overlap between two topological edge states. We show the energy spectrum as a function of μ in Fig.3(b), where the topological edge states are found for $|\mu/t| < 1$.

Winding number: We make a unitary transformation of $H(k)$ by a matrix U given by

$$U \equiv (-i\Gamma_{0x} + \Gamma_{0z} + \Gamma_{x0} - \Gamma_{xy}$$
$$+ i\Gamma_{yx} + \Gamma_{yz} + i\Gamma_{z0} + i\Gamma_{zy})/2\sqrt{2}. \quad (4)$$

It follows that

$$UHU^{-1} = H_0 \otimes \tau_0, \quad (5)$$

with

$$H_0 \equiv \begin{pmatrix} 0 & q(k) \\ q^*(k) & 0 \end{pmatrix}, \quad (6)$$

and

$$q(k) \equiv t\cos k - \mu - iJ\sin k, \quad (7)$$

where we have used the relations $U\Gamma_{0z}U^{-1} = \Gamma_{x0}$ and $U\Gamma_{zx}U^{-1} = \Gamma_{y0}$. The Hamiltonian reduces to a set of two copies of the two-band model H_0.
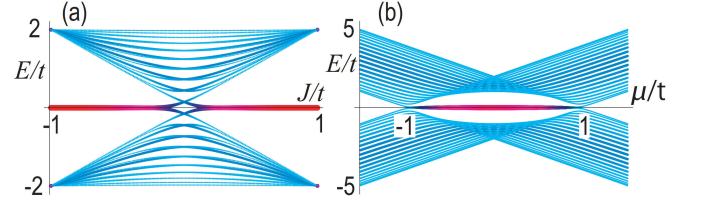

FIG. 3. (a) Energy spectrum as a function of J, where we have set $\mu = 0$. (b) Energy spectrum as a function of μ, where we have set $J = 0.5t$. Red color indicates the topological edge states, while cyan color indicates the bulk states. We have set $L = 20$.

The topological number is the winding number defined by

$$w \equiv \frac{i}{2\pi} \int_0^{2\pi} q^{-1}(k) \frac{dq(k)}{dk} dk. \quad (8)$$

The winding number is $w = 1$ if $q(k)$ encircles the origin anticlockwise in the complex plane made of $\text{Re}[q(k)]$ and $\text{Im}[q(k)]$, while it is $w = -1$ if $q(k)$ encircles the origin clockwise. On the other hand, it is $w = 0$ if $q(k)$ does not encircle the origin. We show the topological phase diagram in the J-μ plane in Fig.1(a). If $|\mu/t| < 1$, the winding number is $w = 1$ for $J > 0$ and $w = -1$ for $J < 0$. On the other hand, $w = 0$ for $|\mu/t| > 1$. It agrees with the number of topological edge states at one edge in the system H_0.

Comparison to the SSH model: The Hamiltonian H_0 could be mapped to the long-range SSH model H_{SSH} with $q_{\text{SSH}}(k) = t_A + t_B e^{-2ik} - \mu e^{-ik}$ by making a unitary transformation,

$$H_{\text{SSH}} = U_{\text{SSH}} H_0 U_{\text{SSH}}^{-1} \equiv \begin{pmatrix} 0 & q_{\text{SSH}}(k) \\ q_{\text{SSH}}^*(k) & 0 \end{pmatrix}, \quad (9)$$

with

$$U_{\text{SSH}} \equiv \begin{pmatrix} 1 & 0 \\ 0 & e^{ik} \end{pmatrix}, \qquad q_{\text{SSH}}(k) = q(k) e^{-ik}. \quad (10)$$

and $t_A = (t - J)/2$, $t_B = (t + J)/2$. However, their topological properties are different, as shown in Figs.1(a) and (b). The difference is understood because the momentum-dependent unitary transformation U_{SSH} is nonlocal.

Indeed, the winding number is transformed as

$$w_{\text{SSH}} \equiv \frac{i}{2\pi} \int q_{\text{SSH}}^{-1}(k) \frac{dq_{\text{SSH}}(k)}{dk} dk$$
$$= \frac{i}{2\pi} \int \left(q^{-1}(k) \frac{dq(k)}{dk} - ik \right) dk = w + 1. \quad (11)$$

It well explains the relation between these two models as in Fig.1(b).

Jackiw-Rebbi zero-energy interface state: We consider a domain wall configuration $J(x)$ in the altermagnet with length L. We assume that it has the same form as in the conventional magnet,

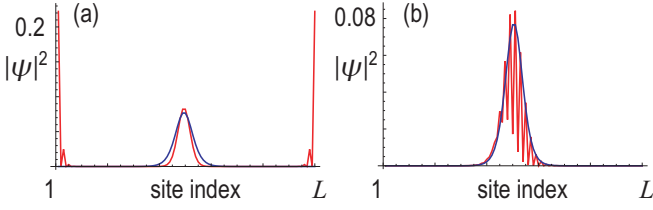$$J(x) = J\sigma_z \tanh\frac{x - L/2 - 1/2}{\xi}, \quad (12)$$

FIG. 4. (a) Spatial profile of the topological interface and edge states base on the Jackiw-Rebbi model. (b) Spatial profile of the topological interface states based on the magnetic domain-wall model. Red curves indicate numerical results based on the tight-binding model, while blue curves indicate analytic solutions based on the Jackiw-Rebbi model. We have set $\xi = 5$ and $J = 0.5t$.

satisfying $\lim_{x \to \infty} J(x) = J$ and $\lim_{x \to -\infty} J(x) = -J$, where the magnetization is flipped without in-plane components. The in-plane component is neglected, which is a good approximation for a very sharp domain wall, $\xi/L \ll 1$. We will discuss the effect of the in-plane canting later in the cases of the Bloch and Néel domain walls.

The gap closes at $k = \pm\pi/2$, $\mu = 0$ and $J = 0$. In its vicinity, the Hamiltonian H_0 is expanded as

$$H_0 = \begin{pmatrix} 0 & \mp tk' - \mu - iJ \\ \mp tk' - \mu + iJ & 0 \end{pmatrix}, \quad (13)$$

where we have defined $k' = k \mp \pi/2$. The Jackiw-Rebbi equations read[35]

$$\{\mp it\partial_x - \mu - iJ(x)\}\psi_B(x) = 0, \quad (14)$$
$$\{\mp it\partial_x - \mu + iJ(x)\}\psi_A(x) = 0, \quad (15)$$

where (ψ_A, ψ_B) is the basis vector of the Hamiltonian H_0 in the coordinate space.

Case (i): The solution is

$$\psi_A(x) = 0, \quad (16)$$
$$\psi_B(x) = \exp\left[\mp\frac{1}{t}\int^x (-J(x') + i\mu)\,dx'\right], \quad (17)$$

for $J > 0$ with $k' = k - \pi/2$, and for $J < 0$ with $k' = k + \pi/2$.

Case (ii): The solution is

$$\psi_A(x) = \exp\left[\mp\frac{1}{t}\int^x (J(x') + i\mu)\,dx'\right], \quad (18)$$
$$\psi_B(x) = 0, \quad (19)$$

for $J < 0$ with $k' = k - \pi/2$, and for $J > 0$ with $k' = k + \pi/2$.

In the case (i), with the use of Eq.(12), we obtain

$$\psi_B(x) = \sqrt{\frac{\Gamma(1/2 + |J|\xi/t)}{\sqrt{\pi}\xi\Gamma(|J|\xi/t)}}\, e^{i\mu x/t} \cosh^{-\frac{|J|\xi}{t}}\frac{x - \frac{L+1}{2}}{\xi}. \quad (20)$$

In the case (ii), we obtain Eq.(20) for $\psi_A(x)$. We show the spatial profile $|\psi(x)|^2 \equiv |\psi_A(x)|^2 + |\psi_B(x)|^2$ by a blue curve in Fig.4(a).
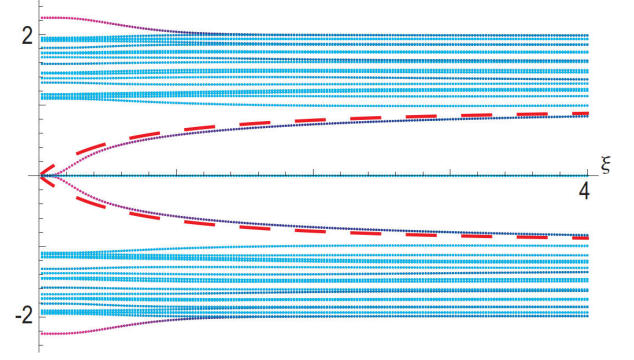

FIG. 5. Energy spectrum as a function of ξ. The red dashed curves indicate analytic solutions (25) based on the first-order perturbation theory. We have set $J = 0.5t$ and $\mu = 0$. Red color indicates the interface states, while cyan color indicates the bulk or edge states.

We also show the spatial profile $|\psi(x)|^2$ obtained numerically based on the tight-binding model by a red curve in Fig.4(a). The tight-binding result consists of the topological interface state at $x = L/2$ and the topological edge states at $x = 1, L$. There are four-fold degenerate topological interface states from $k = \pm\pi/2$ and from the two copies of the Hamiltonian H_0.

One interface state has a half charge

$$\rho(x) = \frac{e}{2}|\psi(x)|^2, \quad (21)$$

according to the standard argument of the Jackiw-Rebbi state[35]. The charge is localized at the domain wall. Hence, the domain wall position is detected by electrical means. Furthermore, it is controlled by applying external electric field along the x direction because the interface states are charged, where the domain wall and the interface states are bounded.

Bloch and Néel magnetic domain walls: The domain wall is actually canted and forms the Bloch or the Néel domain wall instead of the Jackiw-Rebbi type domain wall. The magnetization is

$$J(\sigma_z \cos\theta(x) + \sigma_x \sin\theta(x)) \quad (22)$$

for the Néel domain wall, and

$$J(\sigma_z \cos\theta(x) + \sigma_y \sin\theta(x)) \quad (23)$$

for the Bloch domain wall, where we have set

$$\cos\theta(x) = \tanh\frac{x - 1/2}{\xi}, \quad \sin\theta(x) = \operatorname{sech}\frac{x - 1/2}{\xi}. \quad (24)$$

We estimate the energy of the Bloch and Néel domain walls. We use the first-order perturbation theory[36] in the presence of the term proportional to $\sin\theta(x)$ in Eqs.(22) and (23), where the eigenfunctions do not change but the energy is shifted. The first-order energy displacement is calculated with the use of Eq.(20) as

$$|E| = \int |\psi(x)|^2 \sin\theta(x)\,dx = |J|\frac{\Gamma^2\left(\frac{1}{2} + \frac{J\xi}{t}\right)}{\Gamma\left(1 + \frac{J\xi}{t}\right)\Gamma\left(\frac{J\xi}{t}\right)}, \quad (25)$$

which is independent of the canted direction between the Bloch and the Néel domain walls.

We show the energy (25) as a function of ξ by dotted red curves in Fig.5. They well agree with the numerical results on the energy spectrum in Fig.5, where the first-order perturbation theory and the continuum theory are not assumed. There is a tiny discrepancy at small ξ between the analytical and the numerical results. The numerical result shows a flat dispersion for $|J\xi/t| \ll 1$, while it is linear in the analytic result. It is due to the break down of the continuum approximation. For small ξ, Eq.(25) yields

$$|E| = J\pi\xi/t + o\left((J\pi\xi/t)^2\right). \quad (26)$$

On the other hand, for large ξ, Eq.(25) yields

$$|E|/J = 1 - t/4J\xi + (t/4J\xi)^2/2 + o\left((t/4J\xi)^3\right). \quad (27)$$

The interface states persist for the Bloch and the Néel domain walls but acquire nonzero energy as shown in Fig.4(b), whose spatial profile is well coincident with that of the Jackiw-Rebbi solution as depicted by a blue curve. It is understood as follows. The contribution of the in-plane component is tiny for a sharp domain wall. In this regime, we can treat the in-plane Hamiltonian as a perturbation term. Hence, the eigenstates remains as they are but the energy is modified in the first-order perturbation theory.

A comment is in order. The domain wall width is controlled by introducing the easy-axis anisotropy term $-AS_z^2$ to the system, which favors the spin pointing up or down. The domain wall width becomes smaller for larger easy-axis anisotropy.

2D model: An actual sample has a finite width W. We consider a two-dimensional generalization of the model, where the Hamiltonian is given by

$$H_2 = (t\cos k_x + t\cos k_y - \mu)\Gamma_{0z} + (J\sin k_x)\Gamma_{zx}. \quad (28)$$

It reduces to the one-dimensional model with the replacement of the chemical potential μ by $\mu(k_y) = \mu' - t\cos k_y$. We study a nanoribbon geometry based on Hamiltonian (28). We find that there emerge 4 zero-energy topological edge states for odd width nanoribbons. Examples for the width $W = 2, 3, 4$ are shown in Fig.2(b), (c) and (d).

This even-odd effect with respect to W is understood as follows. The Hamiltonian is actually made of two copies as in Eq.(5). In the vicinity of the zero energy, each Hamiltonian is well approximated by two chains with length W at $x = 1$ and L, each of which is constituted of topological edge states. The effective Hamiltonian of one chain is given by

$$H_{\text{eff}} = t\sum_{y=1}^{W-1}\left(\hat{f}_y^\dagger\hat{f}_{y+1} + \hat{f}_{y+1}^\dagger\hat{f}_y\right), \quad (29)$$

for $W \geq 2$, where $\hat{f}_y$ is an annihilation operator of the topological edge state. The energy spectrum is obtained as $E_{\text{eff}}(j) = t\cos(2\pi j/W + 1)$ with $j = 1, \cdots W$. There is one zero-energy state for odd W and no zero-energy state for even W. As a result, by considering two copies of the model and two edges, we have 4 zero-energy states for a nanoribbon with odd W.

Discussions: We have argued that the domain wall position can be detected and controlled by electric field. Altermagnets have zero-net magnetization, which enables ultrahigh density magnetic memories. Magnetic racetrack memory based on the p-wave altermagnet will be a basis of future magnetic devices. Electrical control does not produce Joule heating because current is not applied, which has advantage comparing to the current induced domain wall motion such as by the spin-transfer torque[21, 22]. Our results will open a new field of energy-saving spintronics based on p-wave altermagnets.

[1] L. Smejkal, A. H. MacDonald, J. Sinova, S. Nakatsuji and T. Jungwirth, Anomalous Hall antiferromagnets, Nat. Rev. Mater. 7, 482 (2022).

[2] L. Smejkal, J. Sinova, and T. Jungwirth, Beyond Conventional Ferromagnetism and Antiferromagnetism: A Phase with Non-relativistic Spin and Crystal Rotation Symmetry, Phys. Rev. X, 12, 031042 (2022).

[3] Libor Šmejkal, Jairo Sinova, and Tomas Jungwirth, Emerging Research Landscape of Altermagnetism, Phys. Rev. X 12, 040501 (2022).

[4] Amar Fakhredine, Raghottam M. Sattigeri, Giuseppe Cuono, and Carmine Autieri, Interplay between altermagnetism and nonsymmorphic symmetries generating large anomalous Hall conductivity by semi-Dirac points induced anticrossings, Phys. Rev. B 108, 115138 (2023).

[5] Teresa Tschirner, Philipp Keler, Ruben Dario Gonzalez Betancourt, Tommy Kotte, Dominik Kriegner, Bernd Buechner, Joseph Dufouleur, Martin Kamp, Vedran Jovic, Libor Smejkal, Jairo Sinova, Ralph Claessen, Tomas Jungwirth, Simon Moser, Helena Reichlova, Louis Veyrat, Saturation of the anomalous Hall effect at high magnetic fields in altermagnetic RuO$_2$, APL Mater. 11, 101103 (2023).

[6] Toshihiro Sato, Sonia Haddad, Ion Cosma Fulga, Fakher F. Assaad, Jeroen van den Brink, Altermagnetic anomalous Hall effect emerging from electronic correlations, arXiv:2312.16290

[7] Miina Leivisk Javier Rial, Anton Badura, Rafael Lopes Seeger, Ismaa Kounta, Sebastian Beckert, Dominik Kriegner, Isabelle Joumard, Eva Schmoranzerov Jairo Sinova, Olena Gomonay, Andy Thomas, Sebastian T. B. Goennenwein, Helena Reichlov Libor Smejkal, Lisa Michez, Tom Jungwirth, Vincent Baltz, Anisotropy of the anomalous Hall effect in the altermagnet candidate Mn5Si3 films, arXiv:2401.02275

[8] J. Krempask, L. Šmejkal, S. W. D'Souza, M. Hajlaoui, G. Springholz, K. Uhlov F. Alarab, P. C. Constantinou, V. Strocov, D. Usanov, W. R. Pudelko, R. Gonzez-Herndez, A. Birk Hellenes, Z. Jansa, H. Reichlov Z. Šob, R. D. Gonzalez Betancourt, P. Wadley, J. Sinova, D. Kriegner, J. Min, J. H. Dil and T. Jungwirth, Altermagnetic lifting of Kramers spin degeneracy,

Nature 626, 517 (2024).

[9] Suyoung Lee, Sangjae Lee, Saegyeol Jung, Jiwon Jung, Dong-han Kim, Yeonjae Lee, Byeongjun Seok, Jaeyoung Kim, Byeong Gyu Park, Libor Šmejkal, Chang-Jong Kang, Changyoung Kim, Broken Kramers Degeneracy in Altermagnetic MnTe, Phys. Rev. Lett. 132, 036702 (2024).

[10] O. Fedchenko, J. Minar, A. Akashdeep, S.W. D'Souza, D. Vasilyev, O. Tkach, L. Odenbreit, Q.L. Nguyen, D. Kutnyakhov, N. Wind, L. Wenthaus, M. Scholz, K. Rossnagel, M. Hoesch, M. Aeschlimann, B. Stadtmueller, M. Klaeui, G. Schoenhense, G. Jakob, T. Jungwirth, L. Smejkal, J. Sinova, H. J. Elmers, Observation of time-reversal symmetry breaking in the band structure of altermagnetic RuO_2, Science Advances 10,5 (2024) DOI: 10.1126/sciadv.adj4883.

[11] T. Osumi, S. Souma, T. Aoyama, K. Yamauchi, A. Honma, K. Nakayama, T. Takahashi, K. Ohgushi, and T. Sato, Observation of a giant band splitting in altermagnetic MnTe, Phys. Rev. B 109, 115102 (2024)

[12] Zihan Lin, Dong Chen, Wenlong Lu, Xin Liang, Shiyu Feng, Kohei Yamagami, Jacek Osiecki, Mats Leandersson, Balasubramanian Thiagarajan, Junwei Liu, Claudia Felser, Junzhang Ma, Observation of Giant Spin Splitting and d-wave Spin Texture in Room Temperature Altermagnet RuO2, arXiv:2402.04995.

[13] Makoto Naka, Satoru Hayami, Hiroaki Kusunose, Yuki Yanagi, Yukitoshi Motome and Hitoshi Seo, Spin current generation in organic antiferromagnets, Nat. Com. 10, 4305 (2019).

[14] Rafael Gonzalez-Hernandez, Libor Šmejkal, Karel Vborn, Yuta Yahagi, Jairo Sinova, Tomš Jungwirth, and Jakub Železn. Efficient electrical spin splitter based on nonrelativistic collinear antiferromagnetism, Phys. Rev. Lett., 126:127701, (2021).

[15] M Naka, Y Motome, and H Seo, Perovskite as a spin current generator. Phys. Rev. B, 103, 125114, (2021).

[16] Arnab Bose, Nathaniel J. Schreiber, Rakshit Jain, Ding-Fu Shao, Hari P. Nair, Jiaxin Sun, Xiyue S. Zhang, David A. Muller, Evgeny Y. Tsymbal, Darrell G. Schlom & Daniel C. Ralph, Tilted spin current generated by the collinear antiferromagnet ruthenium dioxide, Nature Electronics 5, 267 (2022).

[17] Anna Birk Hellenes, Tomas Jungwirth, Jairo Sinova, Libor Šmejkal, Unconventional p-wave magnets, arXiv:2309.01607.

[18] Kazuki Maeda, Bo Lu, Keiji Yada, Yukio Tanaka, Theory of tunneling spectroscopy in p-wave altermagnet-superconductor hybrid structures, arXiv:2403.17482.

[19] A. Yamaguchi, T. Ono, S. Nasu, K. Miyake, K. Mibu, and T. Shinjo, Phys. Rev. Lett. 92, 077205 (2004).

[20] Stuart S. P. Parkin Masamitsu Hayashi, Luc Thomas, Magnetic Domain-Wall Racetrack Memory, Science 320, 190 (2008).

[21] Gen Tatara and Hiroshi Kohno, Theory of Current-Driven Domain Wall Motion: Spin Transfer versus Momentum Transfer, Phys. Rev. Lett. 92, 086601 (2004).

[22] Gen Tatara, Hiroshi Kohno, Junya Shibata, Microscopic approach to current-driven domain wall dynamics, Physics Reports 468, 213 (2008).

[23] T. Jungwirth, X. Marti, P. Wadley and J. Wunderlich, Antiferromagnetic spintronics, Nature Nanotechnology 11, 231 (2016).

[24] V. Baltz, A. Manchon, M. Tsoi, T. Moriyama, T. Ono, and Y. Tserkovnyak Antiferromagnetic spintronics, Rev. Mod. Phys. 90, 015005 (2018).

[25] Jiahao Han, Ran Cheng, Luqiao Liu, Hideo Ohno and Shunsuke Fukami, Coherent antiferromagnetic spintronics Nature Materials 22, 684 (2023).

[26] Zhuoliang Ni, A. V. Haglund, H. Wang, B. Xu, C. Bernhard, D. G. Mandrus, X. Qian, E. J. Mele, C. L. Kane and Liang Wu , Imaging the Neel vector switching in the monolayer antiferromagnet MnPSe3 with strain-controlled Ising order Nature Nanotechnology 16, 782 (2021).

[27] J. Godinho, H. Reichlov, D. Kriegner, V. Novak, K. Olejnik, Z. Kašpar, Z. Šoban, P. Wadley, R. P. Campion, R. M. Otxoa, P. E. Roy, J. Železnny, T. Jungwirth and J. Wunderlich, Electrically induced and detected Neel vector reversal in a collinear antiferromagnet, Nature Communications volume 9, Article number: 4686 (2018).

[28] Kenta Kimura, Yutaro Otake and Tsuyoshi Kimura, Visualizing rotation and reversal of the Neel vector through antiferromagnetic trichroism, Nature Communications, 13, 697 (2022).

[29] Yi-Hui Zhang, Tsao-Chi Chuang, Danru Qu, and Ssu-Yen Huang, Detection and manipulation of the antiferromagnetic Neel vector in Cr2O3 Phys. Rev. B 105, 094442 (2022).

[30] Rafael M. Fernandes, Vanuildo S. de Carvalho, Turan Birol, Rodrigo G. Pereira, Topological transition from nodal to nodeless Zeeman splitting in altermagnets, Phys. Rev. B 109, 024404 (2024).

[31] Di Zhu, Zheng-Yang Zhuang, Zhigang Wu, and Zhongbo Yan, Topological superconductivity in two-dimensional altermagnetic metals, Phys. Rev. B 108, 184505 (2023).

[32] Yu-Xuan Li and Cheng-Cheng Liu, Majorana corner modes and tunable patterns in an altermagnet heterostructure, Phys. Rev. B 108, 205410 (2023).

[33] Sayed Ali Akbar Ghorashi, Taylor L. Hughes, Jennifer Cano, Altermagnetic Routes to Majorana Modes in Zero Net Magnetization, arXiv:2306.09413

[34] M. Ezawa, Detecting the Neel vector of altermagnet by attaching a topological insulator and crystalline valley-edge insulator arXiv:2403.09150

[35] R. Jackiw and C. Rebbi Phys. Rev. D 13 3398 (1976).

[36] Ryohei Wakatsuki, Motohiko Ezawa, Naoto Nagaosa, Domain wall of a ferromagnet on a three-dimensional topological insulator, Scientific Reports 5, 13638 (2015).